Above-threshold ionization driven by few-cycle spatially bounded inhomogeneous laser fields

P Rueda[1], F Videla[1,2], E Neyra[1] ⓘ, J A Pérez-Hernández[3], M F Ciappina[4,5] ⓘ and G A Torchia[1] ⓘ

[1] Centro de Investigaciones Ópticas (CIOp) CONICET La Plata-CICBA, Camino Centenario y 506 s/n, M. B. Gonnet, CP 1897, Provincia de Buenos Aires, Argentina
[2] Departamento de Ciencias Básicas, Facultad de Ingeniería UNLP, 1 y 47 La Plata, Argentina
[3] Centro de Láseres Pulsados (CLPU), Parque Científico, E-37008 Villamayor, Salamanca, Spain
[4] Institute of Physics of the ASCR, ELI-Beamlines, Na Slovance 2, 182 21 Prague, Czech Republic
[5] ICFO - Institut de Ciencies Fotoniques, The Barcelona Institute of Science and Technology, Av. Carl Friedrich Gauss 3, 08860 Castelldefels (Barcelona), Spain

E-mail: gustavot@ciop.unlp.edu.ar

Abstract

In this work, we study the main features of the photoelectrons generated when noble gas atoms are driven by spatially bounded inhomogeneous strong laser fields. These spatial inhomogeneous oscillating fields, employed to ionize and accelerate the electrons, result from the interaction between a pulsed low intensity laser and bow-tie shaped gold nanostructures. Under this excitation scheme, energy-resolved above-threshold ionization (ATI) photoelectron spectra have been simulated by solving the one-dimensional (1D) time-dependent Schrödinger equation (TDSE) within the single active electron (SAE) approximation. These quantum mechanical results are supported by their classical counterparts, obtained by the numerical integration of the Newton–Lorentz equation. By using near-infrared wavelengths (0.8–3 μm) sources, our results show that very high energetic electrons (with kinetic energies in the keV domain) can be generated, far exceeding the limits obtained by using conventional, spatially homogeneous fields. This new characteristic can be supported considering the non-recombining electrons trajectories, already reported by Neyra and coworkers (Neyra E, *et al* 2018 *J. Opt.* **20**, 034002). In order to build a real representation of the spatial dependence of the plasmonic-enhanced field in an analytic function, we fit the generated 'actual' field using two Gaussian functions. We have further analyzed and explored this plasmonic-modified ATI phenomenon in a model argon atom by using several driven wavelengths at intensities in the order of 10^{14} W cm^{-2}. Throughout our contribution we carefully scrutinize the differences between the ATI obtained using spatially homogeneous and inhomogeneous laser fields. We present the various physical origins, or correspondingly distinct physical mechanisms, for the ATI generation driven by spatially bounded inhomogeneous fields.

Keywords: above-threshold ionization, plasmonics, ultrafast optics

(Some figures may appear in colour only in the online journal)

1. Introduction

High-order harmonic generation (HHG) is one of the most instrumental examples in strong field physics [1, 2]. It is considered the key process to generate coherent radiation in the range of the extreme ultraviolet (XUV) to soft X-Ray spectral range and the workhorse for the generation of attosecond pulses. Invoking the so-called three-step model, both the HHG and the above-threshold ionization (ATI) processes are easy to understand, following an intuitive and simple way

J. Phys. B: At. Mol. Opt. Phys. **53** (2020) 065403

P Rueda *et al*

to describe their underlying physics [3]. The sequence can be defined as follows: (i) the first step corresponds to the ionization of a bound electron, via a tunneling process. This occurs as a consequence of the non-perturbative interaction between the atom and the laser electric field; (ii) the emitted electron travels in the laser-dressed continuum, when it gains a substantial amount of kinetic energy, until the electric field reverses its direction. At this instant, the electron drives back and returns to the vicinity of its parent ion; (iii) finally, and this is might be the most instrumental process of the sequence, the electronic wavepacket has a certain probability of recombination with the nucleus and, in this way, to transform its kinetic energy in harmonic radiation, in the form of photons with a frequency multiple of the incoming one, typically of high order [4]. On the other hand, if the electron elastically rescatters with the parent ion, it gains even more kinetic energy in this subsequent journey, reaching the detector with a much higher velocity, typically of the order of $10U_p$, where U_p is the ponderomotive energy, defined as $U_p = E^2/4\omega^2$, E and ω being the laser electric field peak strength and frequency, respectively.

In the last few years, there has been a tremendous advance in the generation of ultrashort few-cycle carrier-envelope-phase (CEP) stable laser pulses. These kinds of sources are essential to push the limits of the HHG [5, 6]. For example, there exist systems that can deliver sub-two optical cycles, with energies in the mJ regime, in the spectral range of 0.8–2 μm [5, 7, 8]. The interest in obtaining these kinds of pulses mainly relies on the possibility of generating isolated attosecond pulses (IAPs), which would allow the study of atomic and molecular electron dynamics at their native temporal, attosecond scale [3, 9–11]. Additionally, ATI driven by these peculiar sources, has been a particularly interesting research subject, both from the experimental and theoretical viewpoints. The ATI phenomenon, which was experimentally observed more than 30 years ago [12], occurs when an atom or molecule absorbs more photons than the minimum number required to ionize it, with the left-over energy being converted to kinetic energy of the released electron. Energy-resolved ATI spectra are characterized by a sequence of peaks, spaced out by each other by the photon energy. Since the first experimental observation, ATI has been *re-investigated* many times, in order to deeply understand its underlying physics. As it was demonstrated recently, the energy-resolved ATI spectra show very clear low-energy electrons, with kinetic energies below $2U_p$. They account for the majority of the electrons generated in the process and are attributed to a direct ionization process, i.e. to electrons reaching the detector without returning to the region near the ion core. Additionally, since the first experimental realizations, photoelectrons with energies up to $10U_p$ or more have been observed as well. These electrons develop a second energy plateau until reaching the already mentioned $10U_p$ cut-off. They are known as high-energy above-threshold ionization (HATI) electrons, which have been attributed to the rescattering process [13, 14]. Following the simple man's or three-step model, electrons that are freed from the target atom at some well-defined ionization time, t_0, may be driven back to revisit its parent ion. If these returning electrons are back-scattered by the target ion, they can be further accelerated by the laser electric field and emerge as high-energy electrons, reaching kinetic energies up to about $10U_p$. On the other hand, momentum conservation can also be used to explain the kinematics of the re-collision phenomenon. A more complete analysis is reported in [15], where the authors have considered the 2D-electron momentum distribution and demonstrated that the so-called back-scattered rings (BSR) provide useful structural information about the driven target, as well as a solid experimental confirmation that the electrons have been re-scattered backward. Within this scheme, the elastic scattering cross section and the properties of the returning wavepackets can be obtained.

The energy-resolved ATI photoelectron spectra develops a cutoff at the end of the re-scattering plateau. As it was reported in [14], it is possible to associate a particular traveling time to the cutoff energy. Additionally, for energies below than the $10U_p$ cutoff, there are two different electron trajectories (named short and long), each corresponding to a certain (t_0, t_r) pair, where t_r defines the rescattering time. These electrons form the plateau and its yield is primarily determined by the magnitude of the electric field at the ionization time t_0. Finally, during the last few years, ATI generated by few-cycle driving laser pulses has been thoroughly explored and is considered the cornerstone for the absolute CEP characterization [16, 17]. To this end, the so-called backward-forward asymmetry of the momentum-resolved ATI spectrum is measured and thus the absolute CEP value retrieved [15, 18, 19].

In this contribution we study the underlying physics of ATI in a single atom driven by a plasmonic-enhanced spatially bounded inhomogeneous electric field. As was stated, this field results from the interaction between an ultrashort laser pulse and a metal nanostructure. A peculiar characteristic of this field is that it presents a spatial dependence in the same scale as the electron dynamics one (for more details see e.g. [11]) In particular, we explore the ATI features considering an analytic fitting of the actual electric near-field produced by a gold bow-tie shaped nanostructure, when illuminated by a few-cycle laser pulse. Some characteristics of the ATI spectra were reported in [20], where the authors have considered an approximate version of the spatial inhomogeneous electric field, to scrutinize the underlying electron dynamics. In order to accomplish our mission, we numerically solve the time-dependent Schrödinger equation (TDSE) in one dimension (1D) and extract the energy-resolved ATI spectra using a well-established technique [21]. As it was already demonstrated, the 1D-TDSE allows the treatment of a very general set of spatial inhomogeneous fields [20]. Finally, the kinetic energy of both the direct and re-scattered electrons are classically calculated and compared to that obtained from our quantum mechanical approach. Throughout the paper, we highlight the differences between the ATI driven by the homogeneous and inhomogeneous driven fields, for different laser wavelengths.

2. Theoretical approach

In order to carry out the computational simulations, we have considered the polarization of the laser field along the z axis.

J. Phys. B: At. Mol. Opt. Phys. **53** (2020) 065403

P Rueda *et al*

Additionally we modify the interaction term $V_L(x, t)$ to deal with a spatially inhomogeneous field, keeping its dipole condition (for more details see e.g. [20]). Thus, the interaction potential takes the form:

$$V_L(x, t) = - \int E(x, t) \mathrm{d}x. \qquad (1)$$

We describe the spatio-temporal dependence of the electric field through

$$E(x, t) = E_0 f(t) h(x) \sin(\omega t + \phi), \qquad (2)$$

where ϕ refers to the CEP, set as zero for the purpose of this work, and $f(t)$ represents the pulse envelope. We use $\sin^2$-shaped pulses, i.e. we set $f(t) = \sin^2(\omega t / 2n_p)$, where ω is the laser frequency and n_p the number of total optical cycles (o.c.) inside the envelope wave. Finally $h(x)$ represents the non-propagating spatial inhomogeneous field induced in the nanostructure surrounded by a gas, which is described as a sum of two normalized Gaussian functions, as in [22]. Writing $h(x)$ as a Taylor series expansion,

$$h(x) = \sum_i b_i x_i, \qquad (3)$$

we can numerically perform the integral in equation (1), term by term. In order to get convergence, we keep up to the 40th order. Other interesting functions to describe this phenomenon, more complex than the linear one [20],can be seen in [23]. When running our simulations, we assume the rare gas atoms are in the ground state before interacting with the driven field. The 1D-TDSE is then solved numerically by implementing the Crank–Nicolson scheme [20, 24]. To calculate the energy-resolved photoelectron spectra, we use the window function technique developed by Schafer [21]. This observable can be represented by plotting the electron yield versus the energy of the photoelectrons arriving at the detector. Here, two clear plateau regions are observed. The first one, the low energy zone, presents the highest yield. In contrast, the second plateau zone shows less probability, but it is the region where the electron develops its highest kinetic energy.

Additionally, starting from the Lorentz force equation and Newton's second law, we obtain the kinetic energy of the photoelectrons, based on the so-called three-step model. This semi-classical approach is able to satisfactorily reproduce the quantum mechanical direct and rescattered photoelectrons energy cutoffs. In this context, we consider that, in spite of the limitation of the model, the degree of reliability provided by the 1D-TDSE can be considered as a realistic description of the electron dynamics involved in the ATI process. Considering only the electric field of equation (2), and neglecting the action of the magnetic component within a non-relativistic frame, the electron is thrown off to the continuum with no initial velocity, therefore with zero kinetic energy.

From the electron kinematical equations [20], we can extract the temporal intervals of the driven electric field where the ionization and/or recombination take place, in agreement with [6]. Here, we observe that $\frac{\pi}{2} < \omega_0 t < 1.789\,7$ is the interval where the electron returns at least three times close to

the atom; in $1.789\,7 < \omega_0 t < \pi$ the electron comes back exactly once; and for $0 < \omega_0 t < \frac{\pi}{2}$ the electron never comes back.

After returning the first time, it is assumed that the electron elastically rescatters with its parent ion. If this process occurs before the field reaches zero, and at an angle of 180°, the electron is accelerated through almost another half-cycle, gaining much more kinetic energy at the expense of the laser electric field [6, 24]. The maximum predicted kinetic energy is obtained numerically and corresponds to the value of $\approx 10 U_p$. This shows that the larger energies only occur if the rescattering phenomenon takes place. Likewise, the maximum energy achieved by direct ionization corresponds to $2U_p$. We compute the final energy of the measured direct E_d and rescattered E_r electron by means of the following relationships [20, 24]:

$$E_d = \frac{1}{2}[v(t_0) - v(t_f)]^2 \qquad (4)$$

and

$$E_r = \frac{1}{2}[v(t_0) + v(t_f) - 2v(t_r)]^2, \qquad (5)$$

where t_0 and t_r are the ionization and rescattering times, respectively and t_f denotes the end time of the laser pulse. For the calculation of the kinetic energy, we use the spatio-temporal electric field of equation (2). However, note that, in contrast to the quantum approach, the analytic form of the $h(x)$ function can be used to represent the inhomogeneous part of the electric field. The maximum kinetic energies values classically obtained from equations (4) and (5) are in excellent agreement with those extracted from the quantum mechanical calculations (see next section).

3. Results and discussions

The spatial inhomogeneous laser field corresponds to the local near-field distribution around a metallic nanostructure which results in a spatially confined electric field [25, 26]. We retrieve the electric near-field distribution by using a numerical simulation software based on the finite difference time domain (FDTD) method [27]. In order to calculate the near-field distribution, the longitudinal dimension of each bow-tie is set to 175 nm and the separation between the bow-tie apexes to 20 nm. Figure 1 shows the electric near-field amplitude distribution in a range around ± 40 nm centered at the middle of the gap. Here, we use a laser wavelength $\lambda = 800$ nm and an intensity of 10^{11} W cm^{-2}. In order to reduce the complexity of our study, without loosing accuracy, we have considered the cross section between the bow-tie apexes. This point of view simplifies the representation of the electric near-field to one spatial dimension, as it is detailed in figure 1. Additionally, the field distribution is normalized with respect to the strength at point A. The electric field distribution is then constructed by using two Gaussian functions [22]. The maximum associated laser intensity is three orders of magnitude larger
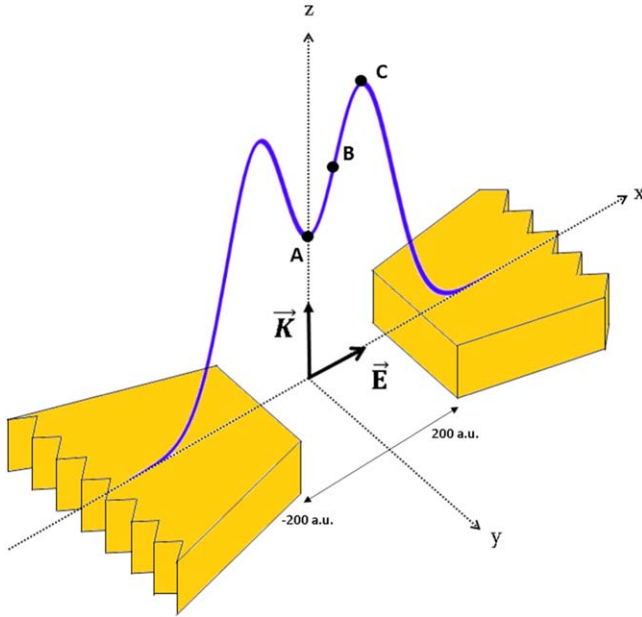
Figure 1. Pictorical representation of the enhanced one-dimensional electric near-field generated by a bow-tie nanostructure under a laser excitation. The points A, B, and C represent the different locations where the target atoms will be placed (see text for more details).

than the excitation laser intensity, i.e. $\sim 10^{14}\,\mathrm{W\,cm^{-2}}$, in fair agreement with other works [28].

Under this simplified scheme, representative of the non-propagating field spatial shape, we point out three different points A, B and C, where we place the target atoms and perform both the quantum mechanical and classical simulations. We focus our analysis on atoms in the framework of the single-active electron (SAE). The target atom, argon, has a covalent radius closest to 2 Angstroms (approx 4 a.u.) a range for which the electric field variation reaches 1% of the applied field, allowing us to neglect this effect. Additionally, it is possible to use the same effective near-field shape for other laser wavelengths, because the numerically calculated field distribution for each wavelength changes only its peak amplitude, leaving its horizontal spatial extension practically unchanged. Finally, note that in this work we suppose the plasmonic-enhanced electric near-field oscillates at ω, the frequency of the laser driving field.

In order to investigate the effects produced by the spatially inhomogeneous laser field, we compare the resulting energy-resolved photoelectron spectra $P(E)$ with the ones obtained when a conventional (spatially homogeneous) field drives the system. To carry out the simulations we employ a sin-squared laser pulse with a total duration of six optical cycles and an intensity of $I = 1 \times 10^{14}\,\mathrm{W\,cm^{-2}}$. In order to assess the role of the laser wavelength, we employ a set of λs, namely 0.8, 1, 1.2, 1.5, 1.8 and 3 μm and we use argon gas as a driven media ($I_p = 15.7596$ eV).

Figure 2 shows the energy-resolved photoelectron spectra corresponding to the homogeneous (left) and inhomogeneous (right) cases, calculated for different driven wavelengths (see caption for details). As it can be seen for the homogeneous case, the spectra shows the well-known characteristic plateaus

corresponding to direct and rescattering electrons, located at $2U_p$ and $10U_p$, respectively. Both cutoff energies follow a λ^2-law, given the fact that $U_p \propto \lambda^2$. It is well known that the first plateau (direct) corresponds to ionized electrons that never return to the region close to the parent ion. This means they move in the laser-dressed continuum after ionization. The second plateau (re-scattering) is originated by electrons that, once ionized, come back to the zone close to the parent ion and rescatter, reaching the detector after moving in the laser-dressed continuum once again. Using classical arguments it is possible to demonstrate that the maximum kinetic energies E_k of the direct and the rescattered electrons are $E_{d_{\max}} = 2U_p$ and $E_{r_{\max}} = 10U_p$, respectively. In a quantum mechanical approach, however, it is possible to find electrons with energies beyond the $10U_p$ cutoff, although their yield drops several orders of magnitude [14]. Experimentally, both mechanisms contribute to the energy-resolved photoelectron spectra and, consequently, any theoretical approach should include them, in order to give a correct description. In that sense, the TDSE, which can be considered as a complete quantum mechanical approach to describe the ATI phenomenon, is able to simulate the $P(E)$ (electron yield) spectra in the whole range of electron energies.

On the other hand, for the inhomogeneous cases, the cutoff positions of both the direct and the rescattered electrons are extended towards larger energies. Particularly, the extension of the cutoff energy for the rescattered electrons is remarkable. For instance, at an excitation wavelength of 1.5 μm (figure 2(e)), there is an important increase of the maximum kinetic energy of the photoelectrons, reaching the keV regime (figure 2(e), right panel). This is in clear contrast to the homogeneous case, where a maximum kinetic energy of around 300 eV is observed (figure 2(e), left panel).

Additionally, from the results corresponding to the inhomogeneous case, a noticeable increasing of the photoelectron yield is also observed. Previously, this effect was observed in the photon flux [22]. In that paper, it was reported that many electron trajectories did not recombine with their parents ions, so a large direct ATI yield could be expected. In this sense, the low probability of recombination, the instrumental step for HHG, can be justified by the low rate of recombining trajectories commented above.

Furthermore, in figure 2 we observe peak-like structures in some of the plateaus. As an example, we can see this effect in the first plateau for all cases, with the exception of figure 2(f) one. On the other hand, in the second plateau, these structures appear in all the homogeneous cases, and might be with the exception of 2(e) and at the inhomogenous cases 2(a), (b) and (d)–(f). The visibility of such features is connected with the behavior of the interference between different electron trajectories and is strongly affected by: (i) the carrier-envelope phase (CEP) [29], (ii) the laser wavelength and (iii) the field inhomogeneity strength and shape. Finally, from the 1D-TDSE results, it is important to remark that the use of spatial inhomogeneous fields for ATI generation would open a new avenue for the production of highly energetic electrons, reaching the keV regime. This could be achieved by tailoring both the spatial and temporal shape of the laser electric field.
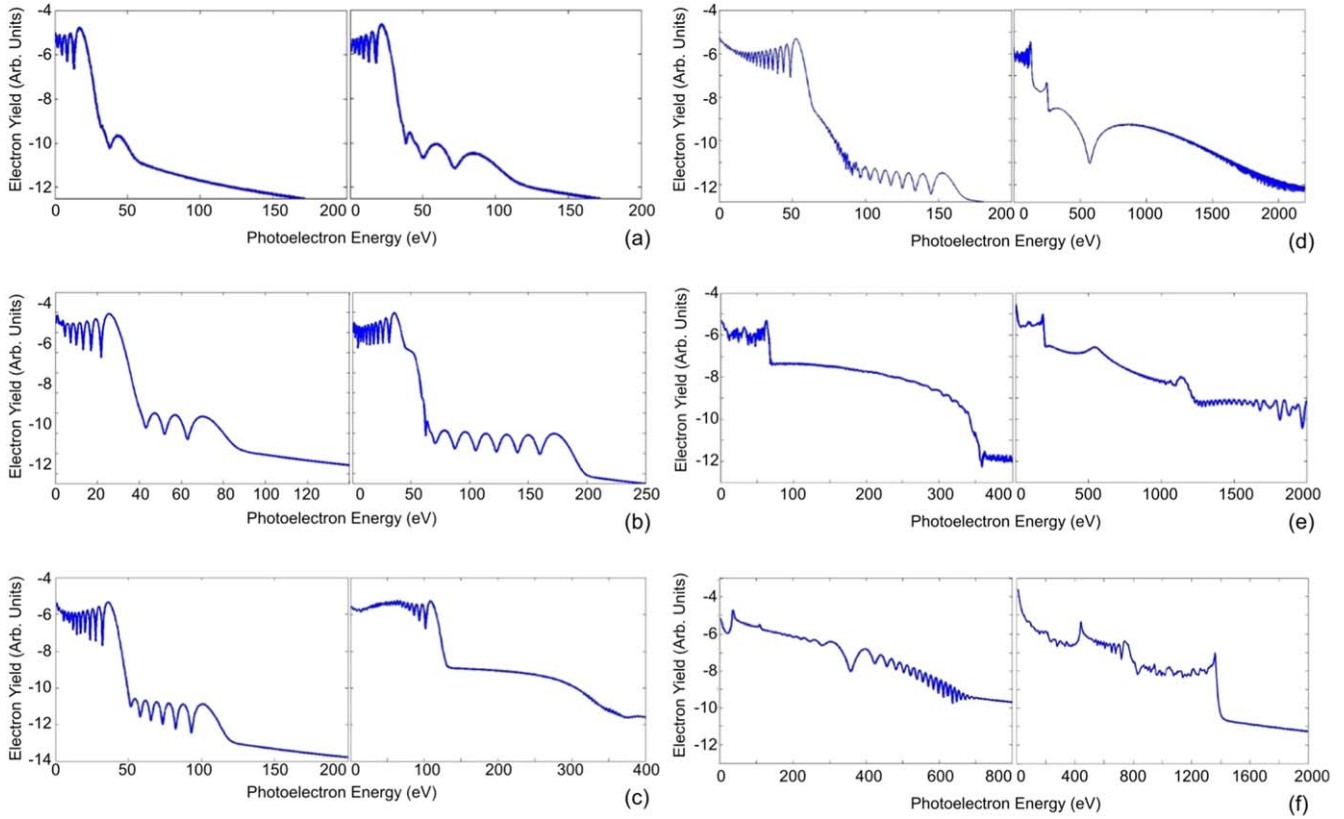
Figure 2. Photoelectron spectra (in logarithmic scale) obtained by solving the 1D-TDSE for target atoms located at the point A, at different wavelengths: (a) 0.8 μm, (b) 1 μm, (c) 1.2 μm, (d) 1.5 μm, (e) 1.8 μm and (f) 3 μm. In each panel, left plot: homogeneous (conventional) case; right panel: inhomogeneous case. We use a sin-squared laser pulse with a total duration of six optical cycles and an intensity of $I = 1 \times 10^{14} \, \mathrm{W \, cm^{-2}}$.

We now explain the extension of the energy-resolved photo-electron spectra using classical arguments. To this end, we integrate the Newton–Lorentz equations for an electron moving in the spatio-temporal field of equation (2). Invoking the three-step model, we can describe the ATI process as follows: an atomic electron at the position $x = 0$ is released or born at a given time, called ionization time t_0, with zero velocity, i.e. $\dot{x}(t_0) = 0$. This electron now moves only under the influence of the oscillating laser electric field (the residual Coulomb interaction is neglected in this model) and will reach the detector either directly or through the rescattering process. In the latter, the recombination time, t_r, is obtained from the condition $x(t_r) = 0$. Once t_i and t_r are computed, the electron kinetic energies are calculated from equations (4) and (5).

In figure 3 we show the classical electron kinetic energies of both the direct (red circles) and rescattered (green circles) electrons, as a function of the ionization and recombination times (for more details see e.g. [20]), for different laser parameters and positions of the target atom (see figure 1).

As it can be seen, a noticeable extension of the cutoff is observed when the laser driven field is spatially inhomogeneous. On the other hand, as is expected, the longer the driven wavelength, the larger the maximum electron kinetic energy. This is because we expect the ponderomotive energy Up scales with λ as a power larger than 2 (see below). Besides, from this picture we note that, when the inhomogeneous character of the applied field is stronger (i.e. the atom is located in point B instead of A, where the field present a larger spatial asymmetry), a larger cutoff can be reached. Similarly, as was previously discussed, larger travel times in the laser-dressed continuum contributes to obtain photoelectrons with higher kinetic energies.

A step further in the analysis is to go deeper in the underlying physics of the electron trajectories, in particular for the spatially inhomogeneous field cases. The travel time of the electrons is noticeably different for these electric fields. As a consequence, and putting the emphasis in the short electron trajectories case, the electron is ionized at earlier times and the recombination step takes place at a later one. In this way it spends more time in the laser-dressed continuum acquiring more energy from the laser electric field. Consequently, higher values of the kinetic energy are gained. A similar behavior with the photo-electrons was observed recently in above-threshold photoemission (ATP) using metal nanotips. According to the model presented in [30], the localized near-fields modify the electron motion in such a way to allow sub-cycle dynamics 'quenching' the quiver radius, and increasing in this way the production of direct photoelectrons. In the present work, however, we consider both direct and re-scattered electrons and the characterization of the their dynamics results much more complex. Nevertheless, the higher kinetic energy of the rescattered electrons is a clear consequence of
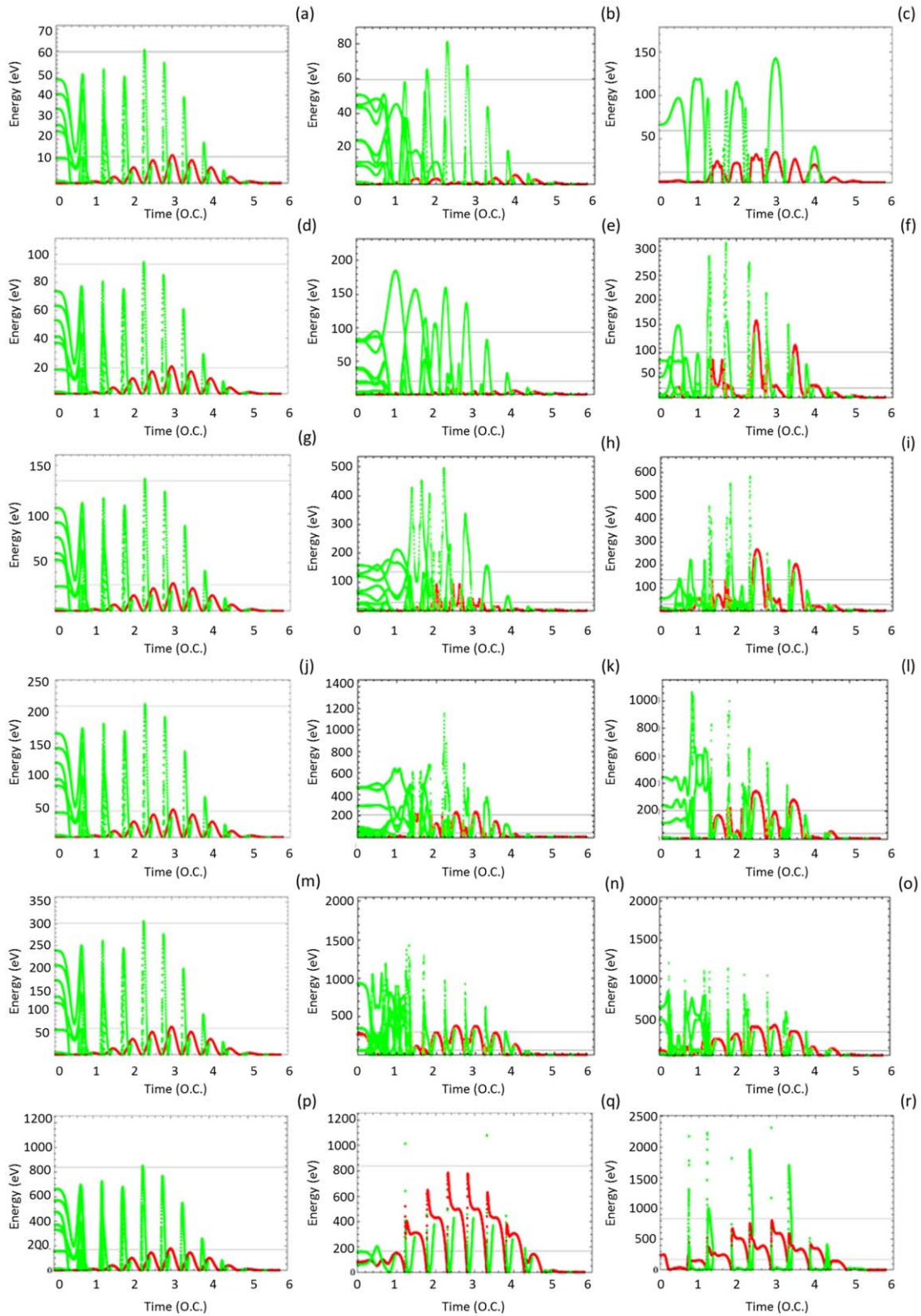
Figure 3. Classical electron kinetic energies for both direct and rescattered electrons, as a function of the ionization and recombination times, and for different laser wavelengths and positions of the target atom (see figure 1). The different panels are organized as follows: leftmost panels: spatial homogeneous driven field; center panels: spatially inhomogeneous driven field at point A and rightmost panels: spatially inhomogeneous driven field at point B. The wavelengths used are: (a), (b), (c) 0.8 μm; (d), (e), (f) 1 μm; (g), (h), (i) 1.2 μm; (j), (k), (l) 1.5 μm; (m), (n), (o) 1.8 μm;(p), (q), (r) 3 μm. The horizontal grey lines represent the energy for direct and re-scatter photo-electrons driven by an homogeneous field.
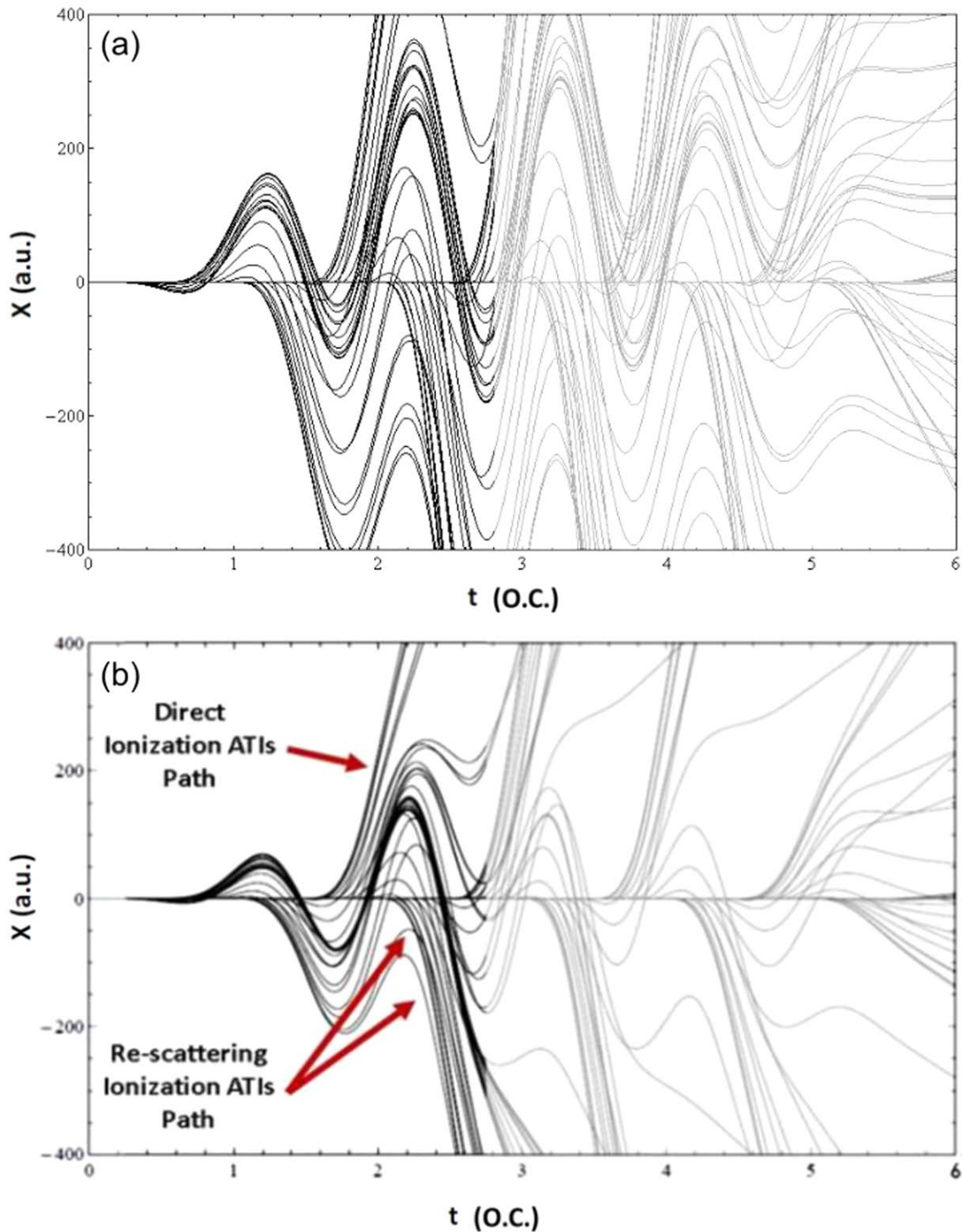
Figure 4. Classical electron trajectories for spatially homogeneous (a) and spatially inhomogeneous (b) fields. The driven laser wavelength is set to 3 μm. The red arrows point out the regions where the direct and re- scattering processes take place in the first part of the laser pulse. As it can be seen, both direct and rescattered electrons appear for this particular spatially inhomogeneous electric field.

the strong modifications of the laser electric field, i.e. due to its spatial inhomogeneity character, in the region where the electron dynamics takes place.

In order to confirm the aforementioned features of the photoelectrons under the spatial inhomogeneous excitation scheme, classical electron trajectories are presented in figure 4(b), for a driven wavelength of 3 μm [31]. Also, in

order to compare the trajectories for both cases, we add the homogeneous case in figure 4(a). Color change corresponds to approximately half of the laser pulse duration (six cycles). This is so by considering that in the three firsts cycles most of the direct and rescattered electrons are generated. From this plot we can clearly see the direct and rescattered electrons trajectories. These regions are pointed out by red arrows.
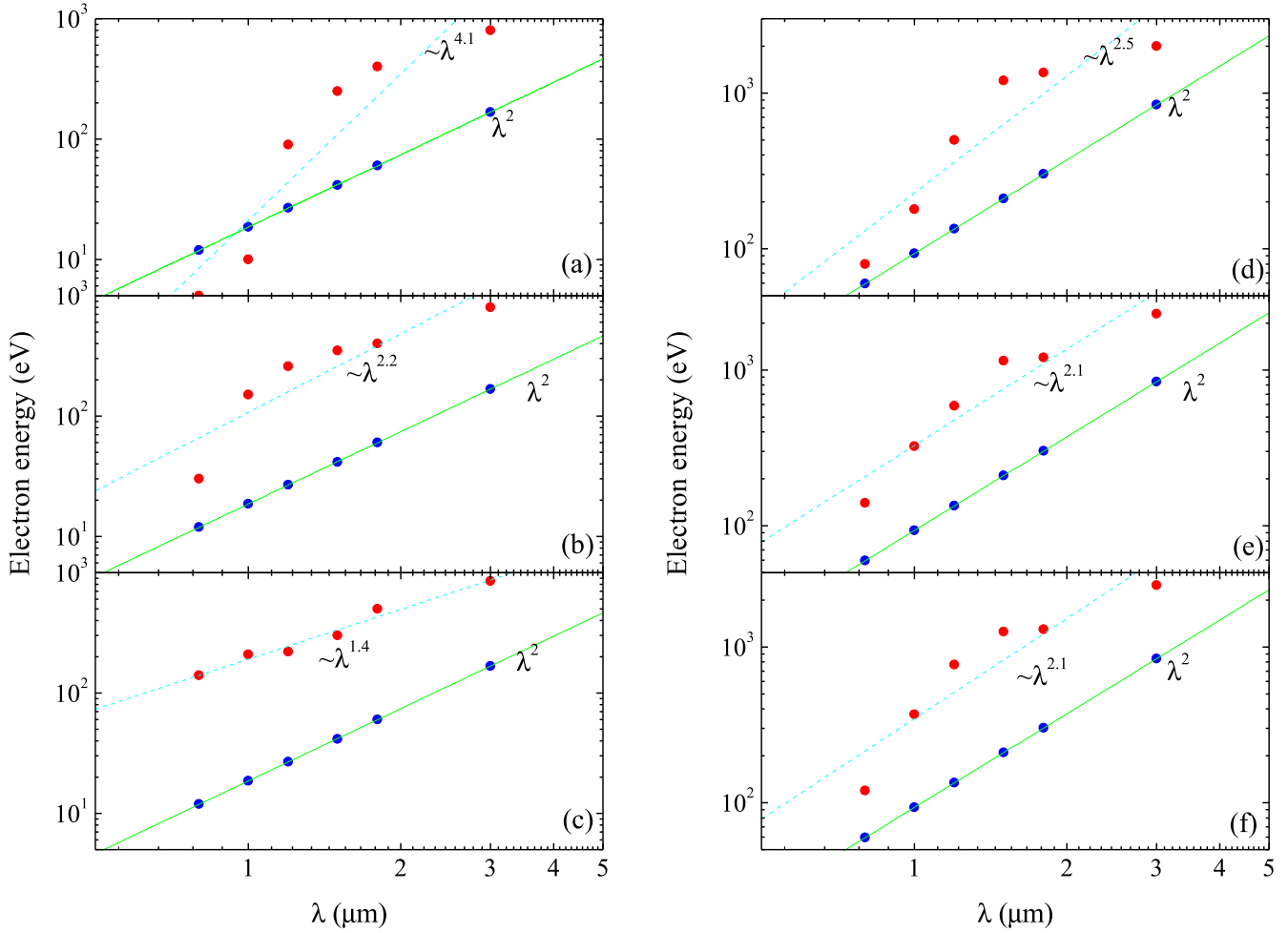
Figure 5. Calculated direct (a), (b), (c) and rescattering (d), (e), (f) cutoff energies versus the driven laser field wavelength (in log-log scale). Panels (a) and (d) correspond to atoms placed at point A; (b) and (e) to point B and (c) and (f) to point C (see figure 1). Solid blue circles: spatially homogeneous (conventional) field; solid red squares: spatially inhomogeneous field. The solid and dash lines correspond to interpolated power laws (see the text for details).

Here, the slope (velocity) corresponding to both the direct and re-scattered electrons is higher. As a consequence, this supports the fact that larger kinetic energies for both kinds of electrons is achieved (see figure 2).

Finally, and in order to complete the analysis of our results, in figure 5 we show, in a log-log scale, the direct and rescattering cutoff energies versus the driven laser wavelength, for different target atom positions and for both spatially homogeneous and inhomogeneous driven fields. We have normalized the field strength for all the points, so a fairer comparison can be made.

On the one hand, we can see that, for homogeneous fields, the position of the target atom (A, B or C) results are irrelevant and both the direct and rescattering cutoff energies show a linear dependence with the driven laser wavelength. This becomes clear from the proportionality between the cutoff energies and λ, $E_{\text{cutoff}} \propto \lambda^2$, for both the direct and rescattered electrons. On the other hand, for the case of spatially inhomogeneous fields, a much more complex dependence is observed. Indeed, the scaling law of both cutoff energies is now a function of the atom target position, as is expected. We could try to find scaling laws for these cutoff

energies, using linear interpolation functions with different slopes. Within this approximation, we can see that, for point A, the cutoff energy of the direct electrons scales as the laser wavelength to the 4th power (figure 5(a)), which makes this point particularly suitable for the production of direct energetic electrons. For the same target atom location, the cutoff energy for the rescattered electrons presents a slightly higher power than the conventional case, ≈ 2.5 (figure 5(b)). In this sense, we confirm the behavior observed by other authors within a simpler spatially inhomogeneous scheme [32, 33].

When we focus on the other atom locations, points B and C, we observe a similar behavior, i.e. the exponent of the λ-power law is higher than the conventional case, with the exception of the case of the direct electrons generated by atoms placed at point C (figure 5(c)). The different exponents of the λ-power law is a result of the shape of the spatial inhomogeneous fields, distinctive for the different atom locations (figure 1). We should mention that, in some energy-resolved photoelectron spectra, it is challenging to find a clear cutoff energy, particularly for longer wavelengths (see figure 2). As a consequence, for these extreme cases, the scaling law has to be taken with caution. Likewise, for all the

studied cases we note a 'saturation' of the cutoff energies for longer wavelengths. This fact is related to the bounded character of electric field created by the nanostructure, when it is excited by the low-intensity incoming laser pulse [22, 25].

Finally, we have compared the cutoff energies from different ionized departure points, in which the field peak strength is renormalized, as a consequence, we have only considered the shape extension of the inhomogeneous electric field to solve the classical energy for the photoelectrons. In particular we have studied the points A and C, and from the analysis we have pointed out that the photoelectrons obtained at large excitation wavelengths (above 1.5 μm) present higher energy than electrons ionized in the point A instead of those electrons ionized at point C. This fact can be understood taking into account the difference observed for the slope and spatial limits of the electric field corresponding to each analyzed point.

4. Conclusions

In this paper we studied the ATI driven by a spatially bounded plasmonic-enhanced field. Energy-resolved photoelectron spectra for an argon model atom are obtained by employing a quantum mechanical (1D-TDSE) model. These results are complemented using a classical approach, based on the Newton–Lorentz equation of motion. This spatially bounded plasmonic-enhanced field results, for instance, when a bow-tie gold nanostructure is illuminated by a low intensity laser field, as a consequence of the formation of surface plasmon polaritons (SPP). Larger direct and rescattered electron kinetic energy cut-offs, as well as higher photoelectron yields, were obtained, compared to the homogeneous (conventional) case. Electrons within the keV regime are obtained, for the largest laser wavelength employed. These unexpected larger kinetic energies can be attributed to the important changes in the electron trajectories, produced by the spatial changes in the driven field. A similar behaviour for both the photon flux and energy was previously observed for HHG as well (see [22]).

Our work shows that spatially inhomogeneous laser fields present an alternative and suitable driver for the generation of highly energetic electrons. Additionally, by tailoring the spatial distribution of the near-field, it would be possible to adjust not only the maximum electron kinetic energies, but also to mould the electron trajectories, following a desired objective.

Acknowledgments

ORCID iDs

E Neyra ◉ https://orcid.org/0000-0002-3602-3330
M F Ciappina ◉ https://orcid.org/0000-0002-1123-6460
G A Torchia ◉ https://orcid.org/0000-0002-6817-5312

References

[1] McPherson A, Gibson G, Jara H, Johann U, Luk T S, McIntyre I A, Boyer K and Rhodes C K 1987 Studies of multiphoton production of vacuum-ultraviolet radiation in the rare gases *J. Opt. Soc. Am.* B **4** 595

[2] Ferray M, L'Huillier A, Li X F, Lompré L, Mainfray G and Manus C 1988 Multiple-harmonic conversion of 1064nm radiation in rare gases *J. Phys. B: At. Mol. Opt. Phys.* **21** L31

[3] Krausz F and Ivanov M 2009 Attosecond physics *Rev. Mod. Phys.* **81** 163

[4] Lewenstein M, Balcou P, Ivanov M Yu, L'Huillier A and Corkum P B 1994 Theory of high-harmonic generation by low-frequency laser fields *Phys. Rev.* A **49** 2117

[5] Schmidt B E *et al* 2010 Compression of 1.8 μm laser pulses to sub two optical cycles with bulk material *Appl. Phys. Lett.* **96** 121109

[6] Paulus G G, Becker W, Nicklich W and Walther H 1994 Rescattering effects in above-threshold ionization: a classical model *J. Phys. B: At. Mol. Opt. Phys.* **21** L703

[7] Driever S *et al* 2013 Tunable 1.62–2 μm near infrared few cycle pulse generation by filamentation *Appl. Phys. Lett.* **102** 191119

[8] Brida D, Manzoni C, Cirmi G, Marangoni M, Bonora S, Villoresi P, De Silvestri S and Cerullo G 2009 Few-optical-cycle pulses tunable from the visible to the mid-infrared by optical parametric amplifiers *J. of Opt.* **12** 013001

[9] Sansone G *et al* 2006 Isolated single-cycle attosecond pulses *Science* **314** 443

[10] Krausz F and Stockman M I 2014 Attosecond metrology: from electron capture to future signal processing *Nat. Phot.* **8** 205

[11] Ciappina M F *et al* 2017 Attosecond physics at the nanoscale *Rep. Prog. Phys.* **80** 054401

[12] Li X F, L'Huillier A, Ferray M, Lompré L and Mainfray G 1989 Multiple-harmonic generation in rare gases at high laser intensity *Phys. Rev.* A **39** 5751

[13] Paulus G G, Nicklich W, Xu H, Lambropoulos P and Walther H 1994 Plateau in above threshold ionization spectra *Phys. Rev. Lett.* **72** 2851

J. Phys. B: At. Mol. Opt. Phys. 53 (2020) 065403

P Rueda *et al*

[14] Becker W, Goreslavski S P, Milošević D B and Paulus G G 2018 The plateau in above-threshold ionization: the keystone of rescattering physics *J. Phys. B: At. Mol. Opt. Phys.* **51** 162002

[15] Morishita T, Le A-T, Chen Z and Lin C D 2008 Accurate retrieval of structural information from laser-induced photoelectron and high-order harmonic spectra by few-cycle laser pulses *Phys. Rev. Lett.* **100** 013903

[16] Paulus G G, Grasbon F, Walther H, Villoresi P, Nisoli M, Stagira S, Priori E and De Silvestri S 2001 Absolute-phase phenomena in photoionization with few-cycle laser pulses *Nature* **414** 182

[17] Sayler A M, Rathje T, Müller W, Ruhle K, Kienberger R and Paulus G G 2011 Precise, real-time, every-single-shot, carrier-envelope phase measurement of ultrashort laser pulses *Opt. Lett.* **36** 1

[18] Milošević D B, Paulus G G, Bauer D and Becker W 2006 Above-threshold ionization by few-cycle pulses *J. Phys. B: At. Mol. Opt. Phys.* **39** R203

[19] Paulus G G, Lindner F, Walther H, Baltuška A, Goulielmakis E, Lezius M and Krausz F 2003 Measurement of the phase of few-cycle laser pulses *Phys. Rev. Lett.* **91** 253004

[20] Ciappina M F, Pérez-Hernández J A, Shaaran T, Biegert J, Quidant R and Lewenstein M 2012 Above-threshold ionization by few-cycle spatially inhomogeneous fields *Phys. Rev. A* **86** 023413

[21] Schafer K J 2008 *Numerical Methods in Strong Field Physics (Springer Series in Optical Sciences)* vol 134 ed T Brabec (New York: Springer) p 111

[22] Neyra E, Videla F, Ciappina M F, Pérez-Hernández J A, Roso L, Lewenstein M and Torchia G A 2018 High-order harmonic generation driven by inhomogeneous plasmonics fields spatially bounded: influence on the cut-off law *J. Opt.* **20** 034002

[23] Han J X, Wang J, Qiao Y, Liu A H, Guo F M and Yang Y J 2019 Significantly enhanced conversion efficiency of high-order harmonic generation by introducing chirped laser pulses into scheme of spatially inhomogeneous field *Opt. Express* **27** 8768–76

[24] Shaaran T, Ciappina M F and Lewenstein M 2012 Quantum-orbit analysis of high-order-harmonic generation by resonant plasmon field enhancement *Phys. Rev. A* **86** 023408

[25] Kim S, Jin J, Kim Y-J, Park I-Y, Kim Y and Kim S-W 2008 High-harmonic generation by resonant plasmon field enhancement *Nature* **453** 757

[26] Schenk M, Krüger M and Hommelhoff P 2010 Strong-field above-threshold photoemission from sharp metal tips *Phys. Rev. Lett.* **105** 257601

[27] RSoft Design Group, Inc 2008 *FullWAVE-Rsoft User Guide* (New York: RSoft Design Group)

[28] Seiffert L, Henning P, Rupp P, Zherebtsov S, Hommelhoff P, Kling M F and Fennel T 2017 Trapping field assisted backscattering in strong-field photoemission from dielectric nanospheres *J. Mod. Opt.* **64** 1096

[29] Krüger M, Schenk M and Hommelhoff P 2011 Attosecond control of electrons emitted from a nanoscale metal tip *Nature* **475** 78

[30] Herink G, Solli D R, Gulde M and Ropers C 2012 Field-driven photoemission from nanostructures quenches the quiver motion *Nature* **483** 190

[31] Kopold R, Milošević D B and Becker W 2000 Rescattering processes for elliptical polarization: a quantum trajectory analysis *Phys. Rev. Lett.* **84** 383

[32] Ahn B *et al* 2017 Attosecond-controlled photoemission from metal nanowire tips in the few-electron regime *APL Photon.* **2** 036104

[33] Hommelhoff P and Kling M F 2015 *Attosecond Nanophysics* (New York: Wiley)